J. Fluid Mech. (1995), vol. 285, pp. 329–347

Barotropic quasi-geostrophic *f*-plane flow over anisotropic topography

By G. F. CARNEVALE[1], R. PURINI[2], P. ORLANDI[3] AND P. CAVAZZA[3]

[1]Scripps Institution of Oceanography, University of California San Diego, La Jolla, CA 92093, USA
[2]Istituto di Fisica dell'Atmosfera, P.le Luigi Sturzo 31, 00144 Roma, Italy
[3]Dipartimento di Meccanica e Aeronautica, Universita di Roma, "La Sapienza," Via Eudossiana 16, 00184 Roma, Italy

(Received 2 November 1993 and in revised form 28 September 1994)

For an anisotropic topographic feature in a large-scale flow, the orientation of the topography with respect to the flow will affect the vorticity production that results from the topography–flow interaction. This in turn affects the amount of form drag that the ambient flow experiences. Numerical simulations and perturbation theory are used to explore these effects of change in topographic orientation. The flow is modelled as a quasi-geostrophic homogeneous fluid on an *f*-plane. The topography is taken to be a hill of limited extent, with an elliptical cross-section in the horizontal. It is shown that, as a result of a basic asymmetry of the quasi-geostrophic flow, the strength of the form drag depends not only on the magnitude of the angle that the topographic axis makes with the oncoming stream, but also on the sign of this angle. For sufficiently low topography, it is found that a positive angle of attack leads to a stronger form drag than that for the corresponding negative angle. For strong topography, this relation is reversed, with the negative angle then resulting in the stronger form drag.

1. Introduction

Large-scale flow over topography in a rotating environment has been subject to very intense investigation owing to the many possible applications in both the atmosphere and the oceans. Numerous studies of flow–topography interaction have been performed with analytical, numerical and laboratory methods. For purposes of analysis and intuitive understanding, many of these studies have focused on models using isolated, circularly symmetric hills. Excellent historical reviews of that work can be found in Huppert & Bryan (1976), Johnson (1978), Bannon (1980), and Verron & Le Provost (1985). For such simplified models, the question of orientation of the topography with respect to the flow does not arise. However, those models point out a basic asymmetry of the flow-over-topography problem, in that vortex tube compression always produces an anticyclone above the topography that advects the fluid around the hill in the anticyclonic direction. We will see below that for asymmetric topographies this basic asymmetry of the flow interacts with the asymmetry of the topography in a way that produces a dependence on the orientation of the topography of vorticity production and of form drag.

Of course, there are already many notable works that examine flow–topography interactions with a model of topography more complicated than the circularly symmetric hill. Merkine & Kalnay-Rivas (1976) consider an elliptical topography with two orientations, cross-stream and along stream. Pierrehumbert & Malguzzi (1984) consider a dipolar topographic forcing (but with a single orientation). Cook & Held (1992) have investigated flow over an elliptical topography, with a single orientation, in a general circulation model. We should also note that there have been many excellent studies of flow over elongated topography in the form of ridges. In most cases, however, the ridge is of infinite extent and oriented perpendicular to the flow. An exception is the study by Boyer (1971) who considers flow over a ridge of infinite extent at an angle to the large-scale flow. This list of examples does not even begin to mention all of the studies with irregular or random topography or those with actual representations of features on the Earth's surface. On the whole, however, there have not been any systematic studies of the effects of orientation of anisotropic topography of finite extent.

As a first step toward a better understanding of the importance of topographic orientation, we have investigated the dependence of form drag and local vorticity distribution over topography on the angle of orientation. Our study revealed the following interesting effect. For an elongated isolated hill, the size of the form drag depends not only on the size of the angle that the hill's horizontal axis makes with the oncoming flow, but also on the sign of that angle. For sufficiently low topography, it is found that a positive angle of attack leads to a stronger form drag than that for the corresponding negative angle. Furthermore, for strong topography, this relation is reversed, with the negative angle then resulting in the stronger form drag. We describe and attempt to explain these results in terms of the fundamental symmetries of the problem and the positions of the relative vortices that are induced by the topography.

For flow in a rotating environment, the simplest model that captures the essential effects of vortex tube compression and stretching is the quasi-geostrophic model. Within the context of that model, in §2, we set up the basic equations for the problem of determining how the local flow around the topography depends on the orientation of that topography with respect to the large-scale flow. In §3, we give the results of simulations that show how the vorticity distribution over the topography depends on the orientation of that topography in the current. In §4, we examine the dependence of the form drag on the topographic orientation, and relate the results to the vorticity distributions described previously in §3. We develop the perturbation theory for the case of weak topography, and compare the predictions to results from the simulations. Furthermore, we present a simple point-vortex model that helps to explain the transition from the behaviour of the form drag as a function of the angle of attack, as observed in the weak topographic regime, to the very different behaviour observed in the strong topographic regime.

2. The model

The variation of the flow with topographic orientation is captured, in simplest form, by the quasi-geostrophic model for a single homogeneous layer under a rigid lid. The first requirement for the validity of this model is that the rotation rate of the environment is sufficiently high so as to dominate local advective processes. Furthermore, we assume that the layer thickness variation is a small fraction of the mean depth.

Let h be the scaled topography given by $h = f\Delta H/H_0$. Here f is the Coriolis parameter, which is twice the rotation rate, Ω, $-H_0$ is the average depth, and ΔH is the height of the bottom above the mean bottom level. Then the quasi-geostrophic evolution equation is given by

$$\frac{\partial q}{\partial t} + J(\psi - Uy, q) = -r\zeta + \nu\nabla^2\zeta. \tag{2.1}$$

Here $\zeta = \nabla^2\psi$, $q = \zeta + h$ is the potential vorticity, U is a constant uniform eastward flow imposed by the boundary conditions, ψ is the flow resulting from the presence of the topography, and J is the Jacobian defined in the usual way. In quasi-geostrophic theory the flow is in geostrophic balance; thus, up to an additive constant, the pressure variation associated with the presence of the topography is simply proportional to the streamfunction: $p = f\rho\psi$, where ρ is the density of the fluid. This is the simplest model which captures the effect of vortex tube stretching due to passage over topographic features. Besides the advection, we have also included two viscous effects: a bottom drag due to Ekman pumping, and a horizontal diffusion of relative vorticity. For a systematic derivation of the quasi-geostrophic evolution equation see Pedlosky (1987).

We need to define a model of a confined asymmetric topography. The studies of Verron & Le Provost (1985) were performed with a Gaussian-shaped topography, which we extend here to the elongated form:

$$h(x, y) = h_0 e^{-(x'^2/a^2 + y'^2/b^2)}, \tag{2.2}$$

where the coordinates x' and y' are just the old coordinates x and y rotated by the angle of attack of the topography with respect to the oncoming stream, as defined in figure 1. Specifically

$$x' = x\cos\alpha - y\sin\alpha, \tag{2.3}$$

$$y' = x\sin\alpha + y\cos\alpha, \tag{2.4}$$

where $2a$ and $2b$ are the lengths of the major and minor axes of the ellipse made by the contour of topography at the level with $h(x,y) = e^{-1}$. It will be convenient to designate specific terms for the two ends of the ellipse representing the topography. Accordingly, the upstream end of the ellipse will be referred to as the nose of the topography, and the downstream end as the tail. Also we will refer to the line of points on the surface of the topography along the major axis as the crest of the topography.

In what follows, we non-dimensionalize all lengths by the length of the major axis, $L = 2a$, all velocities by the magnitude of the imposed large-scale velocity, $|U|$, and time by the advective time scale, $T = L/|U|$. Thus the non-dimensional topography h_0, in terms of the dimensional variables, is given by $h_0L/|U|$. A small value of the non-dimensional h_0 implies a relatively shallow topography or a relatively strong flow. In the circularly symmetric case, where $a = b$, our choice of scales for non-dimensionalization and our topography are the same as in Verron & Le Provost (1985).

The basic phenomenon in impulsively started flow over a hill is that, by conservation of potential vorticity, fluid pushed up onto the hill acquires negative vorticity, and the fluid that was pushed off the hill acquires positive vorticity. The negative vorticity over the hill remains over the topography, while the positive vorticity is to a greater or lesser degree shed downstream depending on the strength of the flow and the viscosity. For the circularly symmetric hill, and weak viscosity, Verron & Le Provost (1985) identified two distinct flow regimes separated by the critical value $h_0 = 11$. When the topography is 'weak,' that is, when the flow is strong, most of the positive vortex is shed downstream and the stationary flow is close to the inviscid solution

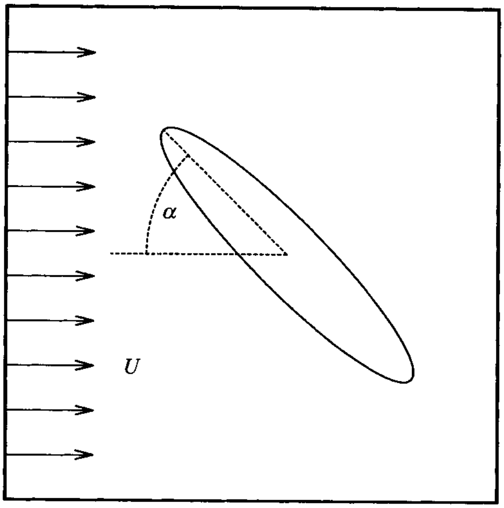

FIGURE 1. Schematic defining the angle of topographic orientation with respect to the flow. The scaled topographic height, defined in the text, is given by $h(x,y) = h_0 \exp(-x'^2/a^2 - y'^2/b^2)$, in coordinates x' and y' that are aligned with the topographic principal axes in a horizontal cross-section. The lengths of the major and minor axes of the contour of topography at level $h(x,y) = e^{-1}$ are $2a$ and $2b$. The angle of attack, α, is defined as the angle (counterclockwise) from the major axis, pointing into the flow, to the negative direction of the large-scale flow. A positive angle of attack, $\alpha = 45°$, is illustrated here.

given by $\zeta = -h$. For 'strong' topography, trapping of the positive vortex can occur, at least temporarily, forming a dipole, which is unstable in the purely inviscid case. In either the strong or weak topography case, if viscous effects are small, most of the cyclone is eventually shed downstream (cf. Huppert & Bryan 1976); but, even then, if there is any viscosity acting on the flow, there will be a remnant of positive vorticity in the stationary flow near the topography. This point will be discussed further below.

In our simulations, we have fixed the length of the semi-minor axis at $b = 0.1$ giving a topography which is far from circular but yet not in the realm of long thin bodies. The boundary condition of uniform flow at infinity presents some difficulties in deciding on the appropriate numerical simulation scheme. We have actually performed our simulations with three different codes with different boundary conditions to check that the effects discussed here are independent of the exact specifications of the boundaries. One of these codes was a finite difference code with a channel geometry with Orlanski (1976) radiation conditions in the downstream direction. The other two codes were spectral. One was run with doubly periodic boundary conditions and the other had an artificial spatial filter which destroyed vorticity far from the centre of the topography. All the results reported below were found for all three different codes and thus appear, at least qualitatively, to be independent of the details of the boundary conditions. This was also checked by doubling the domain size and the filter radius while keeping the resolutions fixed. Thus the phenomena reported below appear local, limited to the region where the confined topography is centred. Also, questions of sensitivity to computational resolution were tested by running all simulations both at resolutions 64×64 and 128×128, with additional key tests at resolution 256×256.

Finally, we must specify the values of the viscous coefficients in the evolution equation (2.1). When considering stationary flow, the inviscid solution is somewhat uninteresting from the point of view of form drag because, as a manifestation of D'Alembert's paradox, there turns out to be no drag at all in that case, as has been pointed out in Bannon (1980) and elsewhere. In other words, if the perturbation flow is stationary and confined (so that there is no possibility of transferring energy into the flow or to infinity), then there can be no energy input for there is no energy sink (see Batchelor 1967). Thus we have to decide on what non-zero values to give to the viscous coefficients r and ν. To limit our search of parameter space, we have decided to set $\nu = 0.01$ and $r = 0.2$, taking these values from the parameter range explored by Verron & Le Provost (1985). In test cases we have varied these values by over an order of magnitude in each direction in order to verify that the phenomena reported are not qualitatively sensitive to these values. In particular, cases with $r = 0$ were checked, since there the trailing cyclone vortex is particularly reduced in strength but is, nevertheless, still present.

3. Structure of the vorticity field

Before proceeding to the question of the form drag, we first illustrate how the flow field over the topography changes with topographic orientation. We will consider only the stationary flow over the elliptical hill forced by the large-scale flow. The results were obtained by simulating impulsively started flow. That is, the flow is initially eastward with speed 1 everywhere. The large-scale component of the flow is maintained at that value thereafter. Initially there is no perturbation field, and since there is no vorticity associated with the large-scale flow, there is initially no vorticity anywhere in the flow. As zero-vorticity fluid is advected onto the topography, it must develop negative relative vorticity to compensate for the positive topographic contribution to the conserved potential vorticity, $q = \zeta + h$. Similarly, fluid advected off the hill must develop positive vorticity. Thus the earliest stage of evolution involves the creation of negative vorticity on the upstream side of the hill and positive vorticity on the downstream side. The later stages of evolution and, in particular, the final stationary flow depend on the strength of the topography. Here we shall take two extreme cases, $h_0 = 1$ and $h_0 = 100$, to illustrate the results for 'weak' and 'strong' topography. As we shall demonstrate, the value $h_0 = 1$ is well within the regime of linear perturbation theory. The larger value $h_0 = 100$ is chosen to be well beyond the transition to nonlinear effects and also to be well above the minimum strength needed for Taylor column formation.

3.1. *Weak topography*

The stationary patterns of relative vorticity for the case $h_0 = 1$ for four different angles of attack are shown in figure 2. For all of these cases, the local or perturbation flow due to the presence of the topography is weak in the sense that the lines of flow or the contours of total streamfunction (not shown) are all nearly parallel to the large-scale flow direction. However, the problem can be analysed in terms of the patterns of relative vorticity. First consider the anticyclone fixed above the hill. Its strength is less than that achieved in the inviscid solution, $\zeta = -h$. The anticyclone is also not perfectly elliptical. Instead, it is relatively larger in magnitude on the upstream side than on the downstream side. The negative vorticity peak is strongest at $\alpha = 90°$ (coming up to 95% of the value of the topography maximum) and weakest for $\alpha = 0°$, and *vice versa* for the positive vorticity. For all angles of attack, there is a peak of positive relative vorticity downstream of the negative vorticity peak.

To help understand these results, consider the fluid element which comes from upstream, crosses the peak of the topography, and then moves downstream. A fluid element approaching from upstream has zero relative vorticity, and, for each 'step' that it takes going uphill, it acquires exactly enough negative vorticity to balance the positive topographic contribution in the conservation of the potential vorticity. Thus for inviscid flow the stationary potential vorticity is exactly zero everywhere with relative vorticity being exactly anticorrelated with the topography, $\zeta = -h$. With viscosity, however, the relative vorticity generated on the fluid element by the topographic effect also dissipates continuously. Thus, when this fluid element reaches its highest point on the topography, its relative vorticity will be weaker in strength than it would have been inviscidly. Then, as it descends the hill, the positive vorticity generated by the conservation of potential vorticity more than cancels the relative vorticity remaining from its climb with the destructive effects of viscosity acting. Thus, net positive relative vorticity must result on the descent. Of course, the positive relative vorticity on the fluid element will continue to diminish as it moves downstream. Of all the cases shown in figure 2, the ascent to the top of the hill by the fluid element is shortest for $\alpha = 90°$. In that case, there is little time for viscosity to act during the ascent and descent. Hence, the anticyclone peak will be strong, and the cyclone weak. In contrast, in the case with $\alpha = 0°$, the excursion to the top is the longest, and hence the effect of viscous decay on the vorticity is the greatest, and the anticyclone will be relatively weak, while the cyclone will be relatively strong.

3.2. *Strong topography*

The structure of the vorticity field in the strong topography case, $h_0 = 100$, contrasts greatly with that in the weak case. The final stationary configurations for the relative vorticity field in this case, for the same four angles of attack shown for the weak topography case, are shown in figure 3. The negative vortex is no longer nearly elliptical. For all the attack angles, the negative vortex is more concentrated at one end of the topography, and the positive vortex is now no longer simply trailing on the x-axis. Even though the negative vortex is now, at most, only 30% of the peak amplitude of the topography, the topography is so strong that the nonlinear term $J(\psi, \zeta)$ competes with the large-scale advection. The negative vortex here is intense enough to strongly displace the trailing positive vortex from the positive x-axis. In varying α from large negative angles to positive angles, we see the peak of the cyclone displaced from the nose of the topography on the trailing side of the topography, to the tail end on the leading side. For the same variation of α, we see the peak of the anticyclone displaced from the tail to the nose of the topography.

4. Form drag in the stationary flow

Topographic form drag is the net force exerted on the flow by the topography along the direction of the large-scale flow. In terms of the streamfunction, which in quasi-geostrophic theory is proportional to the pressure field, the drag, up to a factor of the mean fluid mass per unit area, is given by

$$D = \int h \frac{\partial \psi}{\partial x} \mathrm{d}x \mathrm{d}y \qquad (4.1)$$

(cf. Bannon 1985; Carnevale & Frederiksen 1987). Thus, we see that an enhanced pressure gradient on one side of the topography relative to the other yields a net force on the topography.

Considering the drag in the case of stationary flow, we first check that the drag in

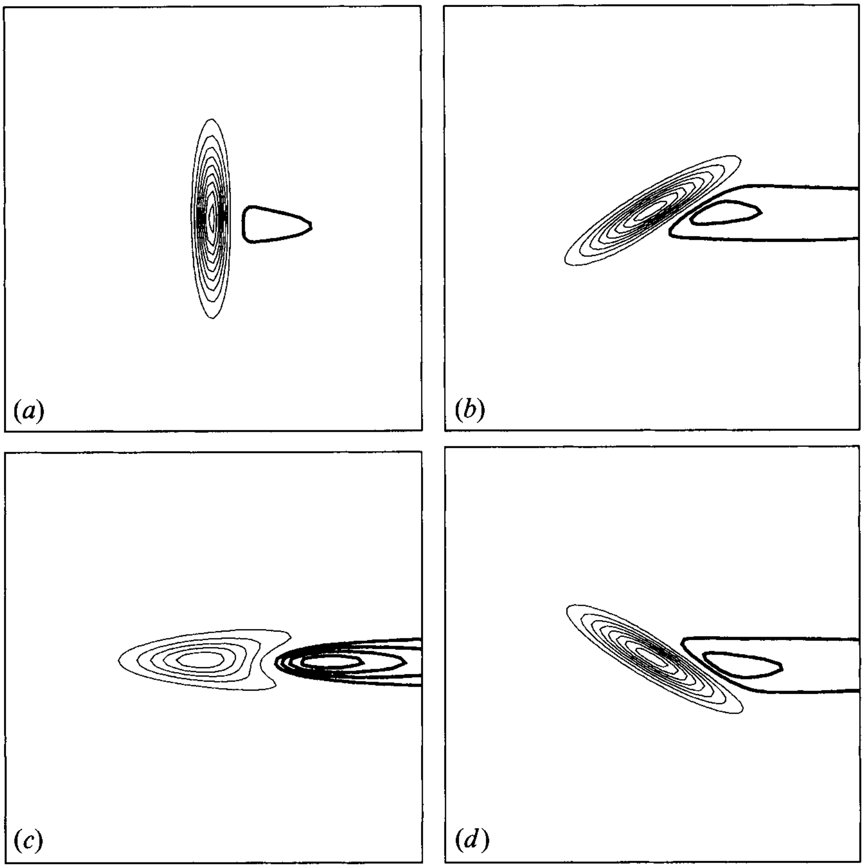

FIGURE 2. Contour plots of the stationary relative vorticity field for the weak topography case, $h_0 = 1$, for various angles of attack. Panels (*a–d*) represent the stationary vorticity field for flow over the elliptical topography for the angles of attack $\alpha = -90°, -30°, 0°$ and $+30°$ respectively. The thick curves correspond to positive vorticity levels spaced 0.05 units apart, while the thin curves correspond to negative vorticity levels spaced 0.1 units apart. The zero vorticity level is not drawn. Only the central region of size 3 × 3, of the full computational domain of 5 × 5, is shown.

the inviscid case is zero as discussed above. The solution to the inviscid problem is given by $q = 0$, that is, $\nabla^2\psi = -h$. Substitute $-\nabla^2\psi$ for h directly in the expression for D and integrate by parts. All that remains after the integration is a boundary term at infinity that vanishes. Next, we turn to numerical results for the stationary states with viscosity. As in the case where we considered the structure of the vorticity field, we will see that the behaviour of the drag is rather different in the weak and strong topography limits.

4.1. *Weak topography*

In figure 4(*a*), we show the drag as a function of the attack angle for the case $h_0 = 1$. The results were obtained from a series of simulations in which the angle of attack was varied from $-90°$ to $+90°$ in 5° increments. Since the form drag is always negative, opposing the large-scale flow, we plot its magnitude. The form drag is greatest when the long axis of the topography is perpendicular (i.e. $\alpha = \pm 90°$) rather than parallel ($\alpha = 0°$) to the flow. The graph of the drag is not symmetric about $\alpha = 0°$. It appears that the form drag is stronger for a positive angle of attack

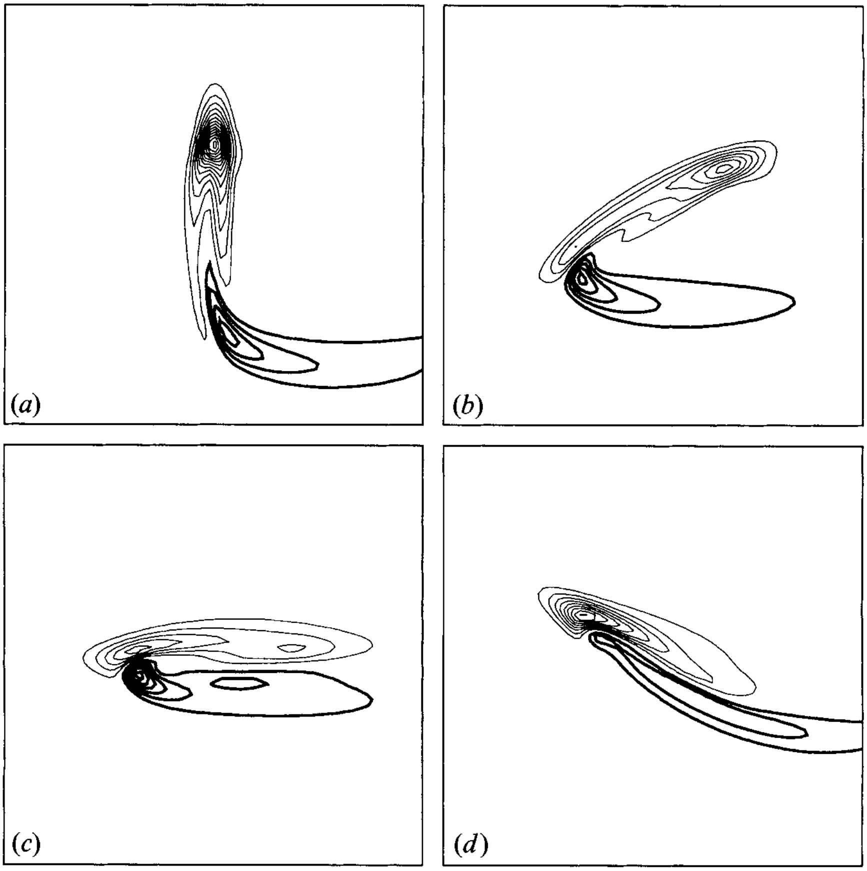

FIGURE 3. Contour plots of the relative vorticity field for the strong topography case, $h_0 = 100$. Panels (*a–d*) represent the stationary vorticity field for flow over the elliptical topography for the angles of attack $\alpha = -90°$, $-30°$, $0°$ and $+30°$ respectively. The thick/thin curves correspond to positive/negative vorticity levels spaced 2.0 units apart. The zero vorticity level is not drawn. Only the central region of size 3×3, of the full computational domain of 5×5, is shown.

than for a negative angle of the same magnitude. In figure 4(*b*), we plot the relative variation of that difference, that is, we plot $(|D(\alpha)| - |D(-\alpha)|)/|D(\alpha)|$, where $D(\alpha)$ is the form drag for a given angle of attack. The figure shows that the difference is greatest when the size of the attack angle is about 20°, with a 2% variation at that angle. For somewhat higher topographies ($h_0 \approx 20$), the relative variation reaches about 20%, as we shall see below.

For the weak topography case, form drag dependence on attack angle can be predicted from perturbation theory. To examine the effects of weak topography, we begin by rewriting the stationary form of equation (2.1) as

$$U\frac{\partial \zeta}{\partial x} + r\zeta - \nu\nabla^2\zeta = -U\frac{\partial h}{\partial x} - J(\psi, \zeta + h). \tag{4.2}$$

Note that since we are dealing with the non-dimensionalized equations, U is actually just the sign of the dimensional large-scale flow. We assume the primary balance for weak topography is between the terms on the left, which are linear in the vorticity, and the first forcing term on the right, $-U\partial h/\partial x$. This permits us to treat the quadratically nonlinear Jacobian term as a small perturbation. It also means that at

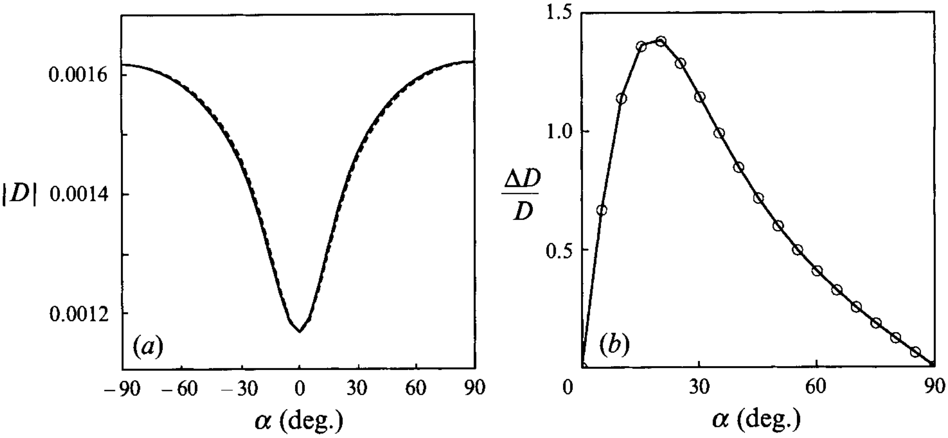

FIGURE 4. Form drag from weak topography perturbation theory for $h_0 = 1$. These calculations were made for doubly periodic boundary conditions. (*a*) The solid curve is the absolute value of the stationary form drag from the fully nonlinear simulation. The dashed curve is the prediction of the lowest-order perturbation theory (see equation (4.5) for $D^{(2)}$). (*b*) The open circles mark the results for the relative variation of the difference between the drag at positive and negative angles of attack for the fully nonlinear simulations. The values given are $100(D(\alpha) - D(-\alpha))/D(\alpha)$. The solid curve shows the prediction for this same quantity of the perturbation theory truncated at next to lowest order, that is, with $D \approx D^{(2)} + D^{(3)}$.

lowest order the streamfunction is linear in the topography, and all succeeding terms are of higher integral order. Thus we write

$$\zeta = \zeta^{(1)} + \zeta^{(2)} + \zeta^{(3)} + \dots, \tag{4.3}$$

where $\zeta^{(n)} = O(h_0^n)$.

The form drag can also be calculated order by order. Directly from the formula (4.1) and the fact that the streamfunction at lowest order is linear in the topography, we see that the form drag is quadratic in the topography at lowest order. Thus the perturbation series for the form drag will be

$$D = D^{(2)} + D^{(3)} + D^{(4)} + \dots. \tag{4.4}$$

Using the Fourier transform in space, we can readily obtain the lowest-order contribution to the drag (see the Appendix for details):

$$D^{(2)} = -U \int \frac{k_x^2 d_k |h_k|^2}{k^2(U^2k_x^2 + d_k^2)} \frac{\mathrm{d}^2 k}{(2\pi)^2}, \tag{4.5}$$

where $\boldsymbol{k}$ is the Fourier wavevector and $d_k = r + \nu k^2$.

It is difficult to apply this perturbation theory, meant for the infinite domain, directly to the simulations with the channel and radiation boundary conditions or the spatially filtered simulation. However, for simulations with periodic boundary conditions, the result is simply a discretization of the continuous formulas. Although the quantitative values are somewhat different from the case with the spatial filter, qualitatively they are the same. In figure 4(*a*), we compare the actual result for the dependence on α for the full nonlinear doubly periodic calculation with the lowest-order result. We see that the linear theory, $D^{(2)}$, shown as a dashed curve, does account for most of the form drag with $h_0 = 1$. We will show that the small difference is due to the first nonlinear term $D^{(3)}$, but let us first note that the lowest-order form drag, $D^{(2)}$, is symmetric in the attack angle. In fact, this will be the case for any topography with a reflection symmetry. To begin with, we show the dependence on the attack angle explicitly. We can define the attack angle either with reference to the angle between the line of symmetry or perpendicular to it. Then we can write $h(x,y;\alpha) = \phi(x',y')$, where x' and y' are just the rotated coordinates defined previously in equations (2.3) and (2.4). A reflection symmetry corresponds to the fact that either $\phi(x,y) = \phi(-x,y)$ or $\phi(x,y) = \phi(x,-y)$. We shall write the Fourier transform of $h(x,y;\alpha)$ as $\hat{h}_{\boldsymbol{k}}(\alpha)$. By using the fact that rotations do not change area, this Fourier transform is found to be

$$h_{\boldsymbol{k}}(\alpha) = \hat{\phi}(k'_x,k'_y), \tag{4.6}$$

where $\hat{\phi}(k_x,k_y)$ is the Fourier transform of $\phi(x,y)$, and

$$k'_x = k_x \cos\alpha + k_y \sin\alpha, \tag{4.7}$$

$$k'_y = -k_x \sin\alpha + k_y \cos\alpha. \tag{4.8}$$

By direct substitution in equation (4.5), we have

$$D^{(2)}(\alpha) = -U \int \frac{k_x^2 d_k |\hat{\phi}(k'_x,k'_y)|^2}{k^2(U^2k_x^2 + d_k^2)} \frac{\mathrm{d}^2k}{(2\pi)^2} \tag{4.9}$$

$$= -U \int \frac{k_x^2 d_k |\hat{\phi}(k_x\cos\alpha + k_y\sin\alpha, -k_x\sin\alpha + k_y\cos\alpha)|^2}{k^2(U^2k_x^2 + d_k^2)} \frac{\mathrm{d}^2k}{(2\pi)^2}. \tag{4.10}$$

Thus,

$$D^{(2)}(-\alpha) = -U \int \frac{k_x^2 d_k |\hat{\phi}(k_x\cos\alpha - k_y\sin\alpha, k_x\sin\alpha + k_y\cos\alpha)|^2}{k^2(U^2k_x^2 + d_k^2)} \frac{\mathrm{d}^2k}{(2\pi)^2}. \tag{4.11}$$

If $\phi(x,y) = \phi(-x,y)$, which implies $\hat{\phi}(-k_x,k_y) = \hat{\phi}(k_x,k_y)$, then the substitution $k_x \rightarrow -k_x$ shows that $D^{(2)}(-\alpha) = D^{(2)}(\alpha)$. If $\phi(x,y) = \phi(x,-y)$, then the same point is demonstrated by the change of variables $k_y \rightarrow -k_y$.

These results show that the asymmetry in the form drag, as seen in figure 4, must come from higher-order terms in the perturbation theory. We shall next demonstrate that for $h_0 = 1$ the second term in the perturbation series captures the observed deviation from symmetry very well. That term, $D^{(3)}$, is derived in general form in the Appendix. If the topography has the point reflection symmetry $h(x,y) = h(-x,-y)$, as is the case for the elliptical topography, then the expression for $D^{(3)}$ simplifies, and we have

$$D^{(3)} = -U^3 \int 2 d_p d_q q^2 k_x^2 p_x q_x b_{\boldsymbol{k}} b_{\boldsymbol{p}} b_{\boldsymbol{q}} \mathscr{D}_{\boldsymbol{kpq}}, \tag{4.12}$$

where

$$b_{\boldsymbol{k}} \equiv \frac{h_{\boldsymbol{k}}}{k^2(U^2k_x^2 + d_k^2)}, \tag{4.13}$$

and

$$\mathscr{D}_{\boldsymbol{kpq}} = \hat{\boldsymbol{z}} \cdot \boldsymbol{p} \times \boldsymbol{q} (2\pi)^2 \delta(\boldsymbol{k} + \boldsymbol{p} + \boldsymbol{q}) \frac{\mathrm{d}^2k}{(2\pi)^2} \frac{\mathrm{d}^2p}{(2\pi)^2} \frac{\mathrm{d}^2q}{(2\pi)^2}, \tag{4.14}$$

as shown in the Appendix.

If, in addition to the symmetry of reflection in a point, the topography is also symmetric to reflection through a line, then we can show that $D^{(3)}(\alpha) = -D^{(3)}(-\alpha)$. For example, if the topography is symmetric about the y'-axis, then $h_{k_x,k_y}(\alpha) =$

$\hat{\phi}(k'_x, k'_y) = \hat{\phi}(-k'_x, k'_y) = h_{-k_x,k_y}(-\alpha)$. Thus, a change of variables in which all k_x, p_x, q_x change sign (note that $\hat{z} \cdot \boldsymbol{p} \times \boldsymbol{q}$ changes sign), in the expression for $D^{(3)}(-\alpha)$, shows that the integrand is simply the negative of that in the expression for $D^{(3)}(\alpha)$. Similarly if $h_{k_x,k_y}(\alpha) = h_{k_x,-k_y}(-\alpha)$, then a change of variables in which all k_y, p_y, q_y change sign, in the expression for $D^{(3)}(-\alpha)$, shows again that the integrand is simply the negative of that in the expression for $D^{(3)}(\alpha)$. By rotation, this result can be further extended to the case for topography with reflection symmetry in any horizontal line. For the periodic boundary condition case, it is again an easy matter to calculate the theoretical drag by discretizing the Fourier representation. In figure 4(*b*), we show the relative difference between the form drag for positive and negative angles of attack (open circles) calculated from the fully nonlinear simulations with periodic boundary condition. These values are compared to the predictions (solid curve) from the perturbation theory truncated at the $D^{(3)}(\alpha)$ contribution. For this weak topography case, the match is almost perfect.

4.2. *Strong topography*

As we increase the amplitude, h_0, of the topography, the perturbation theory can be expected to fail. In two series of experiments, in which the angle of attack was fixed at ±30° respectively, the topography amplitude was varied from 1 to 150. The absolute values of the stationary form drag for these experiments are plotted in figure 5(*a*). The solid/dashed curve corresponds to the experiments with attack angle $+/-30°$. Firstly, we note that for the range of topography roughly from $h_0 = 1$ to $h_0 = 15$, the form drag for both curves is approximately a quadratic function of h_0. This is what one would expect in a weak topography regime where $D^{(2)}$, the lowest-order approximation to the form drag, would dominate. Also note that, in this region, the strength of the form drag for the positive angle is stronger than that for the negative angle. Near $h_0 = 15$ there is a transition to a new regime where the scaling with topography no longer follows the quadratic law. In the strong topography regime, the drag seems to increase with topography amplitude roughly as $h_0^{0.3}$. Also in the strong topography regime, the relation between the form drag for positive and negative angles has reversed, with negative angles of attack corresponding to stronger form drag than positive angles. This last point is emphasized in figure 5(*b*), where the relative difference in form drag strength between the plus and minus 30° cases is plotted as a function of topographic strength.

As an example of the functional dependence of the form drag on angle for a case of strong topography, we plot this relation for the case of $h_0 = 100$ in figure 6(*a*) (solid curve). There have been several papers which discuss in part the theory of strong topographic forcing (cf. Pierrehumbert & Malguzzi 1984); nevertheless, we have not been able to predict the shape of this form drag curve. We note that this curve is somewhat broader about $\alpha = 0°$ than the corresponding curve for $h_0 = 1$ in figure 4(*a*). As an aid to judging the symmetry and smoothness of the curve, we have also plotted the symmetric dashed curve corresponding to $A \sin^2 \alpha + B \cos^2 \alpha$, where A and B were chosen so that the two curves would have the same extremal values. In figure 6(*b*), we plot the relative difference in strengths between positive and negative angles of attack. The shape of the curve is similar to that shown in figure 4(*b*) except, of course, for the sign since in this regime the negative angles correspond to stronger form drag. Here we see that the maximum difference is about −18% at around attack angle $|\alpha| = 20°$. This is a great deal stronger than the $h_0 = 1$ case, but similar in magnitude to the $h_0 = 15$ case(see figure 5*b*), which is still in the regime where the positive attack angle leads to the stronger form drag.

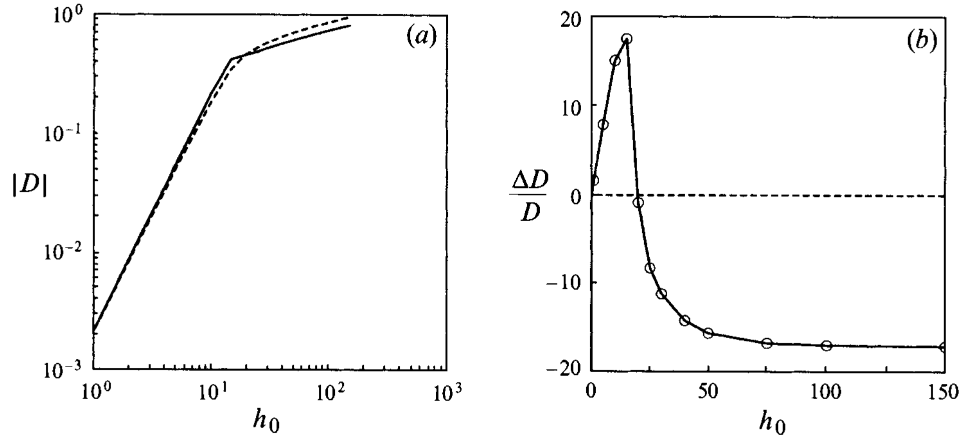

FIGURE 5. Form drag as a function of topographic height. (*a*) Two series of experiments are represented, with the angle of attack, α, fixed in each series at $+30°$ and $-30°$ respectively. The solid/dashed curve shows the absolute value of the stationary form drag from the experiments with $\alpha = +/-30°$. Note that at $h \approx 15$ there is a cross-over from the regime in which the positive angle of attack gives a stronger form drag to the regime with just the reverse relationship. (*b*) The relative difference in form drag strength between the plus and minus 30° cases is plotted as a function of topographic strength (the dashed line is simply the zero level).

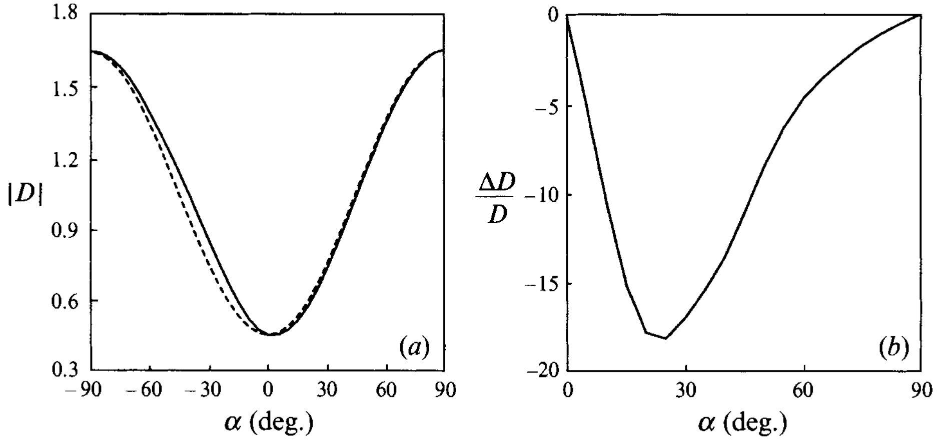

FIGURE 6. Form drag for the strong topography case, $h_0 = 100$. These data are taken from simulations using the code with spatial filter. (*a*) The absolute value of the stationary form drag is plotted as a function of attack angle (solid curve). This is compared to the fit to the symmetric curve $A\sin^2(\alpha)+B\cos^2(\alpha)$ (dashed curve) with A and B chosen to give a good fit at the extremal values of the data. (*b*) The relative variation of the difference between the drag at positive and negative angles of attack is plotted versus attack angle. Specifically the graph represents $100(D(\alpha)-D(-\alpha))/D(\alpha)$, where $D(\alpha)$ is the form drag for a given angle of attack, α.

The cross-over from the weak to the strong topography regime seems, from figures 5(*a*) and 5(*b*), to occur roughly near $h_0 = 15$. As we noted above in §3, when $h_0 = 1$ the total streamfunction is only slightly perturbed from that for uniform flow, but for topographies with amplitudes such as $h_0 = 100$, a Taylor column, i.e. a region of recirculating closed streamlines, exists. It is tempting to try to associate the transition of the form drag behaviour from the weak to the strong limits with the occurrence of the Taylor column. However, the formation of Taylor columns occurs in these simulations for topographic amplitudes above roughly $h_0 = 50$, depending somewhat on the angle of attack, and not at $h_0 = 15$. Of course, in the regime from $h_0 = 15$ to $h_0 = 50$, the streamlines are strongly distorted from the unperturbed case of uniform flow even though closed contours do not form. The behaviour of the form drag as a function of topographic height, as well as its dependence on attack angle, are better understood in terms of the structure of the stationary vorticity field, as we will now consider further.

4.3. *Effects of the structure of the vorticity field*

An examination of the distribution of relative vorticity over the topography, as discussed in §3, can provide us with some physical insight into the behaviour of the form drag. First we consider why, in the weak topography case, the drag is stronger for the positive angle of attack than for the negative angle of the same magnitude. In the perturbation theory, we noted that the lowest-order form drag does not have this asymmetry, and it is necessary to go to the next order to capture this effect. This higher-order effect results from the nonlinear advection produced by the Jacobian, $J(\psi, \zeta)$. Physically this is related to the tendency of the negative vorticity over the topography to displace the positive vortex in an arc in the clockwise direction about the centre of the topography. In the $\alpha = -30°$ case, in figure 2(*b*), the negative vortex is displaced away from the crest of the topography and away from the region of negative vorticity. This results in a weaker induced pressure gradient compared to what it would have been without this angular displacement. In the $\alpha = +30°$ case, in figure 2(*d*), the negative vortex is displaced toward the crest of the topography and toward the region of negative vorticity. Thus the form drag is stronger for the positive-α case than for the negative-α case.

Given the above analysis for the weak topography case, how can we understand the transition to what we have called the strong topography regime in which the form drag is stronger for the negative angle of attack than for the positive angle? As noted above, this effect is not directly related to the formation of Taylor columns. Instead, the answer will be found in the relative positions of the vortices with respect to each other and to the topography. Figure 7 displays data gathered from a series of experiments representing topographies with amplitudes from $h_0 = 1$ to $h_0 = 40$, and to angles of attack $\alpha = \pm 30°$. The positions of the peak of positive relative vorticity (triangles) and negative relative vorticity (dots) are shown over ellipses which represent the topography. For $h_0 = 1$, the positive peak vorticity is located slightly below the x-axis, directly downstream of the centre of the topography. As h_0 increases, the displacement of the positive vorticity peak is rather different for the two topographic orientations. For the $\alpha = -30°$ case, the peak of positive vorticity simply moves further toward the nose of the topography but always remains on the downstream side. For the $\alpha = +30°$ case, the positive vorticity peak is displaced in an arc. Between $h_0 = 10$ and $h_0 = 15$, this peak crosses over the crest of the topography, moving from the downstream to the upstream side. From $h_0 = 15$ to $h_0 = 40$, the peak is displaced more and more toward the nose of the ellipse, remaining always on the upstream side. This shows that the relevant effect is that for $h_0 \approx 15$ the positive vortex peak crosses over from the trailing side of the topography to the leading side in the $\alpha = +30°$ case, while no such transition occurs in the $\alpha = -30°$ case.

We have found that a simple point-vortex model based on the idea that it is mainly the position of the positive vortex that determines whether we are in the strong or weak topographic regime can capture the transition between these regimes. Consider

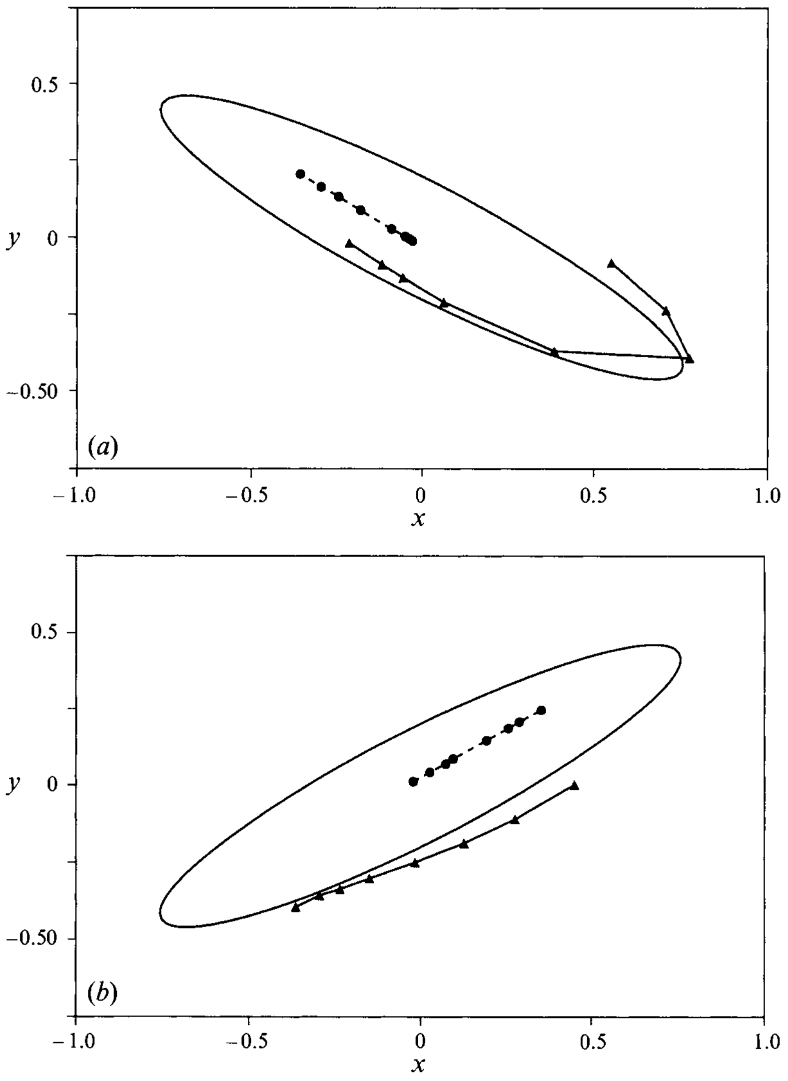

FIGURE 7. Positions of vorticity extrema for different values of the topographic height, h_0. The flow is in the positive x-direction, and the orientation of the topography is indicated by the ellipses, with $\alpha = +30°$ in (*a*) and $\alpha = -30°$ in (*b*). The positions of the positive (negative) vorticity peaks are indicated by the solid triangles (circles). The topographic heights represented are $h_0 = 1, 5, 10, 15, 20, 25, 30$, and 40. In each panel, for $h_0 = 1$, the negative vortex is located approximately over the centre of the ellipse, and the positive peak is just slightly below the x-axis, directly downstream of the centre of the ellipse.

replacing the actual positive and negative vortices by two point vortices, one of each sign. Note that if the negative vortex was exactly at the centre of the topography, then, by symmetry, it can have no contribution to the form drag. For topographic strengths less than $h_0 \approx 15$, the negative vortex is only displaced by a relatively small amount from the centre of the topography; hence, as a first approximation, we neglect its contribution to the form drag and consider only the contribution coming from the positive vortex. Let us further assume that the only effect of increasing the strength of the topography is to change the angular position (θ measured from the x-axis) of the positive vortex. Accordingly, in the model, the positive vortex is taken to be a fixed distance r_0 from the centre of the topography. Thus, we evaluate the contribution to the form drag from a point vortex placed in the position $(r_0 \cos\theta, r_0 \sin\theta)$ as a function of θ. The streamfunction for a point vortex of strength Γ at this position is given by

$$\psi = \frac{\Gamma}{2\pi} \ln(|\boldsymbol{r} - \boldsymbol{r}_0|). \tag{4.15}$$

The resulting form drag is

$$D = \frac{\Gamma}{2\pi} \int \frac{x - x_0}{|\boldsymbol{r} - \boldsymbol{r}_0|^2} h \mathrm{d}x \mathrm{d}y. \tag{4.16}$$

Performing the integration numerically, and varying only the angle θ, we obtain the plots shown in figure 8. The solid graph is the drag, normalized by Γh_0, for the topographic orientation $\alpha = +30°$, and the dashed graph is for $\alpha = -30°$. Keeping in mind that for this model the magnitude of the angle θ is correlated with the height of the topography, we note that for small θ the drag is stronger (i.e. more negative) for positive α than for negative α, and vice versa for large $|\theta|$. Thus, this point-vortex model does capture the same behaviour, at least qualitatively, that we observed in the simulations. Here we have used $r_0 = 0.4$ in the calculations of the drag. The angle θ at which the model passes from the weak to the strong regime is about $\theta = -30°$, which corresponds to placing the point vortex right over the crest of the topography. However, the cross-over point does depend somewhat on the value chosen for r_0. Furthermore, note that as the angle θ becomes very large, a point will be reached at which the point vortex contributes positively to the form drag, as may be intuitively obvious. But, of course, the total drag must be negative, so it is clear that for very large displacements, θ, the contribution of the negative vortex cannot be neglected. To properly capture all aspects of the dependence of form drag on topographic orientation and height would require a far more elaborate model than our one-point model. Nevertheless, this model does capture the essential feature of the form drag's asymmetric dependence on the sign of α in the weak and strong topography regimes.

5. Conclusion

We have explored how the drag that an elongated hill exerts on a flow, in a rotating fluid, depends on the orientation of that hill with respect to the flow direction. As might be expected intuitively, the drag is strongest when the hill's long axis is perpendicular to the flow direction, and it is least when that axis is parallel to the flow. A somewhat less intuitive result is that the strength of the form drag, even for hills with a horizontal cross-section which is symmetric about its long axis, depends not only on the size of the 'angle of attack', but also on the sign of that angle. We related this asymmetric dependence on angle to an interaction between the basic asymmetry in the mechanism of vortex tube compression and the breaking of the circular symmetry of the topography. The advection of zero-relative-vorticity fluid up onto the topography always results in an anticyclone over the topography and this tends to shift the downstream cyclone in an anticyclonic direction, which puts the cyclone either closer to or further from the topography depending on the topographic shape and orientation. Whether a positive angle of orientation results in more or less drag than the corresponding negative angle depends on the height of the hill. We defined a weak and strong (i.e. low and high) topography regime. For weak

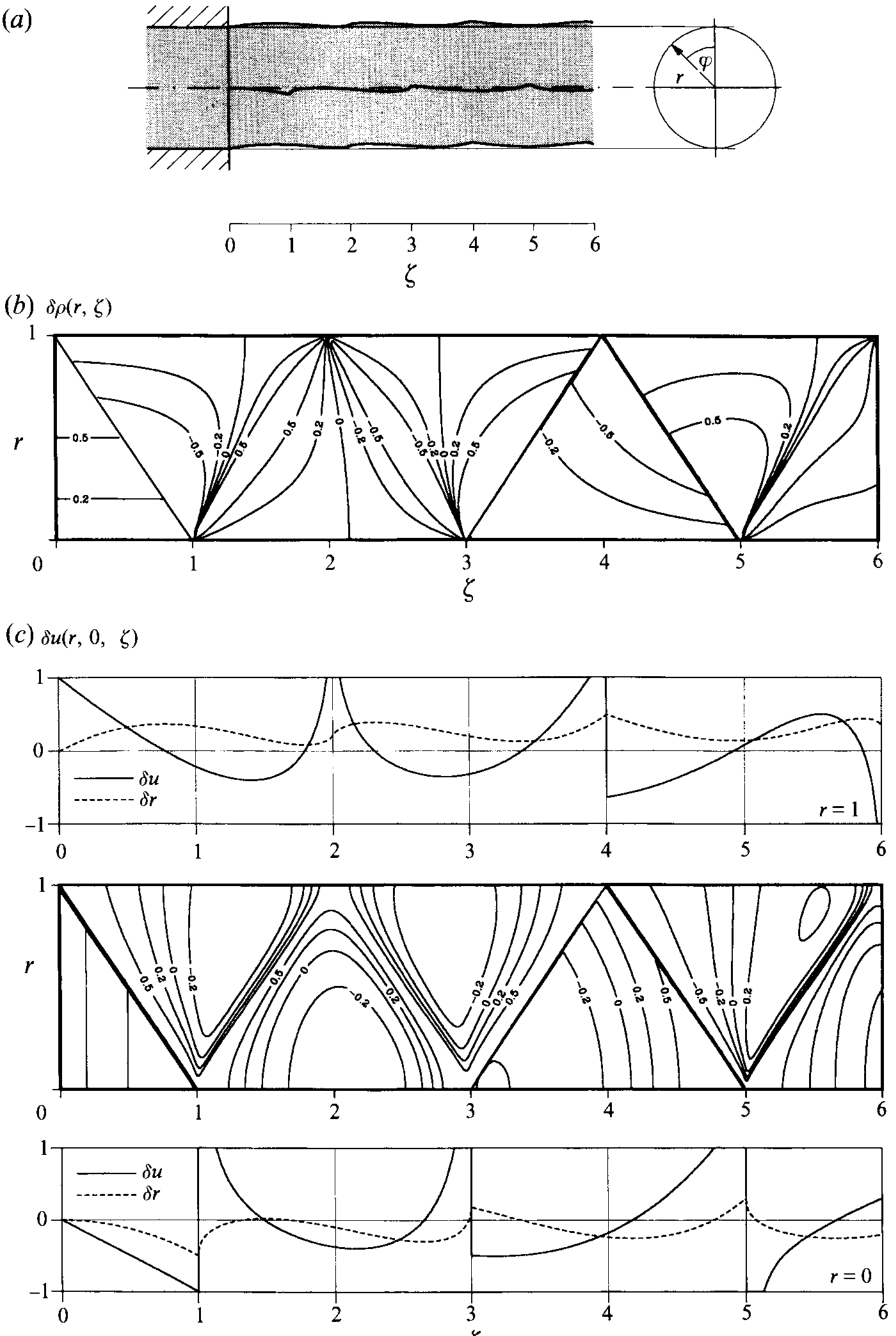

Figure 6. Non-axisymmetric free jet emerging with oblique pressure distribution. (*a*) Problem geometry; (*b*) dimensionless density perturbation $\delta\rho(r,\zeta)$ inside the jet; (*c*) dimensionless perturbation $\delta u(r,\zeta)$ of radial velocity at the jet boundary (top), inside the jet (middle) and on the jet axis (bottom). Dashed curves represent distortions of boundary and axis streamlines.

numerical simulations were performed at the San Diego Super Computer Center. We are grateful for helpful discussions with William Young.

Appendix. Perturbation theory for 'weak' topography

This is a perturbation theory in which the non-dimensional scaled topographic amplitude, h_0, is taken to be the small parameter. Thus we write

$$\psi = \psi^{(1)} + \psi^{(2)} + \psi^{(3)} + \ldots, \tag{A 1}$$

where $\nabla^2\psi^{(n)} = \zeta^{(n)} = O(h_0^n)$.

To evaluate the terms in the perturbation series, we first take the continuous Fourier transform in both x and y of (4.2) to obtain

$$g_k^{-1}\zeta_k = -\mathrm{i}k_x U h_k - J_k(\psi, \zeta + h). \tag{A 2}$$

Recall that in the non-dimensional variables, U is just the sign of the non-dimensional large-scale flow. We carry it along even when raised to an even power simply for book-keeping convenience.

The linear Green function g_k is given by

$$g_k = \frac{1}{\mathrm{i}k_x U + d_k}, \tag{A 3}$$

where $d_k = r + \nu k^2$ and $J_k(A, B)$ is the Fourier transform of the Jacobian of fields A and B. An explicit formula for $J_k(A, B)$ in terms of the Fourier transforms of A and B is given below.

The first- and second-order solutions can then be written as

$$\zeta_k^{(1)} = -\mathrm{i}k_x U g_k h_k, \tag{A 4}$$

and

$$\zeta_k^{(2)} = -g_k J_k(\psi^{(1)}, \zeta^{(1)} + h). \tag{A 5}$$

Using the Fourier transform within the formula for the form drag, we have

$$D = \int h \frac{\partial \psi}{\partial x} \mathrm{d}x\mathrm{d}y = -\int \frac{\mathrm{i}k_x}{k^2} \zeta_k h_{-k} \frac{\mathrm{d}^2 k}{(2\pi)^2}. \tag{A 6}$$

Then by direct substitution of (A 4) into (A 6), we obtain

$$D^{(2)} = -U \int \frac{k_x^2}{k^2} g_k |h_k|^2 \frac{\mathrm{d}^2 k}{(2\pi)^2} \tag{A 7}$$

$$= -U \int \frac{k_x^2(-\mathrm{i}k_x U + d_k)|h_k|^2}{k^2(U^2 k_x^2 + d_k^2)} \frac{\mathrm{d}^2 k}{(2\pi)^2}. \tag{A 8}$$

Notice that the last expression is decomposed into a real and imaginary part. But the form drag is a real quantity. The vanishing of the imaginary part of the integral can be checked by considering the change of sign $\boldsymbol{k} \rightarrow -\boldsymbol{k}$ for the dummy integration variables. Since the topography is real we have the Hermiticity constraint, $h_k^* = h_{-k}$, and so $|h_k|^2$ is unaltered by this sign change. Thus we see that the imaginary part of the integrand changes sign under this sign reversal and so must vanish on integration over the range from $-\infty$ to $+\infty$ for k_x and k_y. Finally we have the result in the text, (4.5).

The next-order term $D^{(3)}$ is given by

$$D^{(3)} = -\int \frac{\mathrm{i}k_x}{k^2}\zeta_{\boldsymbol{k}}^{(2)} h_{-\boldsymbol{k}} \frac{\mathrm{d}^2 k}{(2\pi)^2}, \tag{A 9}$$

and since

$$\zeta_{\boldsymbol{k}}^{(2)} = -g_{\boldsymbol{k}} J_{\boldsymbol{k}}(\psi^{(1)}, \zeta^{(1)} + h), \tag{A 5}$$

this is the lowest-order term to involve vortex–vortex interaction. The Fourier transform of the Jacobian can be represented as

$$\begin{aligned} J_{\boldsymbol{k}}(A,B) &= \int \mathrm{e}^{-\mathrm{i}\boldsymbol{k}\cdot\boldsymbol{r}}\left(\frac{\partial A}{\partial x}\frac{\partial B}{\partial y} - \frac{\partial A}{\partial y}\frac{\partial B}{\partial x}\right)\mathrm{d}^2 r \qquad \text{(A 10)} \\ &= -\int \mathrm{e}^{\mathrm{i}(-\boldsymbol{k}\cdot\boldsymbol{r}+\boldsymbol{p}\cdot\boldsymbol{r}+\boldsymbol{q}\cdot\boldsymbol{r})}(p_x q_y - p_y q_x) A_{\boldsymbol{p}} B_{\boldsymbol{q}} d^2 r \frac{\mathrm{d}^2 p}{(2\pi)^2}\frac{\mathrm{d}^2 q}{(2\pi)^2} \\ &= -\int \hat{\boldsymbol{z}}\cdot\boldsymbol{p}\times\boldsymbol{q} A_{\boldsymbol{p}} B_{\boldsymbol{q}} (2\pi)^2 \delta(-\boldsymbol{k}+\boldsymbol{p}+\boldsymbol{q}) \frac{\mathrm{d}^2 p}{(2\pi)^2}\frac{\mathrm{d}^2 q}{(2\pi)^2}, \end{aligned}$$

where $\hat{\boldsymbol{z}}\cdot\boldsymbol{p}\times\boldsymbol{q} = (p_x q_y - p_y q_x)$ and $\delta(\cdot)$ is the multidimensional Dirac delta function.

Now we can calculate the $D^{(3)}$. Begin by changing the sign of the dummy integration variable, $\boldsymbol{k}$, in (A 9), and substituting for $\zeta^{(2)}$ from (A 5) to obtain

$$D^{(3)} = -\int \frac{\mathrm{i}k_x}{k^2} g_{-\boldsymbol{k}} J_{-\boldsymbol{k}}(\psi^{(1)}, \zeta^{(1)} + h) h_{\boldsymbol{k}} \frac{\mathrm{d}^2 k}{(2\pi)^2}.$$

After introducing the expression for $J_{\boldsymbol{k}}$ and the definition (A 3) for the linear Green function, we obtain

$$\begin{aligned} D^{(3)} &= -U \int \frac{k_x p_x}{k^2 p^2} g_{-\boldsymbol{k}} g_{\boldsymbol{p}} h_{\boldsymbol{k}} h_{\boldsymbol{p}} h_{\boldsymbol{q}} (-\mathrm{i}q_x U g_{\boldsymbol{q}} + 1)\mathscr{D}_{\boldsymbol{kpq}} \qquad \text{(A 11)} \\ &= -U \int k_x p_x [(k_x p_x U^2 + d_k d_p) + \mathrm{i}U(k_x d_p - p_x d_k)] \\ &\quad \times \left(1 - \frac{\mathrm{i}q_x U(-\mathrm{i}q_x + d_q)}{(q_x^2 U^2 + d_q^2)}\right) b_{\boldsymbol{k}} b_{\boldsymbol{p}} h_{\boldsymbol{q}} \mathscr{D}_{\boldsymbol{kpq}}, \qquad \text{(A 12)} \end{aligned}$$

where

$$\mathscr{D}_{\boldsymbol{kpq}} \equiv (\hat{\boldsymbol{z}}\cdot\boldsymbol{p}\times\boldsymbol{q})(2\pi)^2\delta(\boldsymbol{k}+\boldsymbol{p}+\boldsymbol{q})\frac{\mathrm{d}^2 k}{(2\pi)^2}\frac{\mathrm{d}^2 p}{(2\pi)^2}\frac{\mathrm{d}^2 q}{(2\pi)^2}, \tag{4.14}$$

and

$$b_{\boldsymbol{k}} \equiv \frac{h_{\boldsymbol{k}}}{k^2(U^2 k_x^2 + d_k^2)}. \tag{4.13}$$

Expanding (A 11) further leads to an integrand containing several terms, but most of these can be shown to vanish by using the Hermiticity constraint $h_{\boldsymbol{k}} = h_{-\boldsymbol{k}}^{*}$ and the symmetry properties of $\mathscr{D}_{\boldsymbol{kpq}}$. Note that since the Dirac delta function forces $\boldsymbol{k}+\boldsymbol{p}+\boldsymbol{q} = 0$, it follows that $\boldsymbol{k}\times\boldsymbol{p} = -\boldsymbol{k}\times\boldsymbol{q} = \boldsymbol{q}\times\boldsymbol{k}$, and so $\mathscr{D}_{\boldsymbol{kpq}}$ is symmetric under cyclic permutation of the wavevectors $\{\boldsymbol{k},\boldsymbol{p},\boldsymbol{q}\}$, and it is antisymmetric under their pairwise interchange.

After some cancellations and simplifications, the contribution $D^{(3)}$ can be written as a sum of three integrals: $D^{(3)} = I_1 + I_2 + I_3$, where

$$I_1 = -\mathrm{i}U^2 \int k_x p_x (k_x d_p - p_x d_k) b_k b_p h_q \mathscr{D}_{\boldsymbol{kpq}}, \tag{A 13}$$

$$I_2 = 2\mathrm{i}U^4 \int q^2 d_p k_x^2 p_x q_x^2 b_k b_p b_q \mathscr{D}_{\boldsymbol{kpq}}, \tag{A 14}$$

and

$$I_3 = -2U^3 \int q^2 k_x d_p d_q k_x p_x q_x b_k b_p b_q \mathscr{D}_{\boldsymbol{kpq}}. \tag{A 15}$$

If the topography has point reflection symmetry, that is if $h(x,y) = h(-x,-y)$, which implies that $h_{\boldsymbol{k}} = h_{-\boldsymbol{k}}$, as is the case for our elliptical topography, then both I_1 and I_2 vanish. This leaves only I_3, which is the result given in (4.12). Note that since I_3 is antisymmetric with respect to the sign of U, and since $D^{(2)}$ is also antisymmetric, the only effect that changing the sign of U has on $D = D^{(2)} + D^{(3)}$ is to change its sign. This is readily appreciated by considering the geometry of the problem of the ellipse and reversing the sign of U, to see that the two cases are identical subject to a rotation of 180°. On the other hand, since the terms I_1 and I_2 are even in the sign of the large-scale flow, we realize that a lack of point reflection symmetry in the topography breaks the symmetry under large-scale flow reversal, and the magnitude of D will also change when the flow reverses.

REFERENCES

BANNON, P. R. 1980 Rotating barotropic flow over finite isolated topography. *J. Fluid Mech.* **101**, 281–306.

BANNON, P. R. 1985 Flow acceleration and mountain drag. *J. Atmos. Sci.* **42**, 2445–2453.

BATCHELOR, G. K. 1967 *An Introduction to Fluid Dynamics.* Cambridge University Press.

BOYER, D. L. 1971 Rotating flow over long shallow ridges. *Geophys. Fluid Dyn.* **2**, 165–183.

CARNEVALE, G. F. & FREDERIKSEN, J. S. 1987 Nonlinear stability and statistical mechanics of flow over topography. *J. Fluid Mech.* **175**, 157–181.

COOK, K. H. & HELD, I. M. 1992 The stationary response to large-scale oragraphy in a general circulation model and a linear model. *J. Atmos. Sci.* **49**, 525–539.

HART, J. E. 1979 Barotropic quasi-geostrophic flow over anisotropic mountains. *J. Atmos. Sci.* **36**, 1736–1746.

HUPPERT, H. E. & BRYAN, K. 1976 Topographically generated eddies. *Deep-Sea Res.* **23**, 655–679.

JOHNSON, E. R. 1978 Trapped vortices in rotating flow. *J. Fluid Mech.* **86**, 209–224.

MERKINE, L. & KALNAY-RIVAS, E. 1976 Rotating stratified flow over finite isolated topography. *J. Atmos. Sci.* **33**, 908–922.

ORLANSKI, I. 1976 A simple boundary condition for unbounded hyperbolic flows. *J. Comput. Phys.* **21**, 251–269.

PEDLOSKY, J. 1987 *Geophysical Fluid Dynamics,* 2nd edn. Springer.

PIERREHUMBERT, R. T. & MALGUZZI, P. 1984 Forced coherent structures and local multiple equilibria in a barotropic atmosphere. *J. Atmos. Sci.* **41**, 246–257.

VERRON, J. & LE PROVOST, C. 1985 A numerical study of quasi-geostrophic flow over isolated topography. *J. Fluid Mech.* **154**, 231–252.